TiN surface dynamics: role of surface and bulk mass transport processes

J. Bareño[a], S. Kodambaka[b], S.V. Khare[c] , W. Swiech[a], V. Petrova[a], I. Petrov[a], and J.E. Greene[a]

[a]Department of Materials Science and the Frederick Seitz Materials Research Laboratory
University of Illinois, 104 South Goodwin Avenue, Urbana, IL 61801, USA
[b]IBM Research Division, T. J. Watson Research Center, Yorktown Heights, New York 10598, USA.
[c]Department of Physics and Astronomy, University of Toledo, Toledo, OH 43606, USA

Abstract. Transition-metal nitrides, such as TiN, have a wide variety of applications as hard, wear-resistant coatings, as diffusion barriers, and as scratch-resistant and anti-reflective coatings in optics. Understanding the surface morphological and microstructural evolution of these materials is crucial for improving the performance of devices. Studies of surface step dynamics enable determination of the rate-limiting mechanisms, corresponding surface mass transport parameters, and step energies. However, most models describing these phenomena are limited in application to simple elemental metal and semiconductor surfaces. Here, we summarize recent progress toward elucidating the interplay of surface and bulk diffusion processes on morphological evolution of compound surfaces. Specifically, we analyze the coarsening/decay kinetics of two- and three-dimensional TiN(111) islands and the effect of surface-terminated dislocations on TiN(111) steps.

Keywords: Microscopic aspects of nucleation and growth, STM, LEEM.
PACS: 68.55.Ac, 68.37.Ef, 68.37.Nq.

I. INTRODUCTION

Growth of nanostructures, and thin films in general, is a complex phenomenon controlled by the interplay of both thermodynamic and kinetic driving forces. Fundamental understanding of the processes governing the formation and stability of nanostructures can be developed via studies of the dynamics of surfaces at the atomic scale. Prior to the invention of scanning tunneling microscopy (STM) [1] and related scanning probe microscopy tools such as atomic force microscopy (AFM) [2], field ion microscopy (FIM) [3] was the only real-space imaging technique available for resolving individual atoms on surfaces and for studying dynamic processes such as surface diffusion of single adatoms and small two-dimensional (2D) islands [4,5]. Despite the restrictions on the type and size of materials that can be used in FIM studies, which requires high electrical fields and sharp single-crystalline tips, detailed investigations of adatom transport mechanisms have been carried out on a wide variety of metal surfaces [6].

The advent of high-speed variable temperature and pressure STM allows studies of surface dynamics at video rates [7-11] for a wider range of materials. Using STM, *in-situ* studies of the diffusion of adspecies (adatoms and advacancies), kinks, steps, and

2D islands [12-21] are carried out over a wide range of temperatures (20-1500 K). From analyses of the changes in successive images, atomic processes contributing to these phenomena are quantified. The kinetics of nucleation and growth [22,23,24] on crystalline surfaces are also routinely studied in-situ, either in ultra-high vacuum or electrolytic environments. A related tool, the AFM, is also used to study the nucleation and growth kinetics of crystals in a liquid environment [25,26].

Low energy electron microscopy (LEEM) [27] is another surface-sensitive analytical technique (complementary to STM) in which a coherent, low energy electron beam (typically 1-100 eV) illuminates the sample; the electrons undergo diffraction and are captured by an objective lens to form a real-space image of the surface. Using a contrast aperture, diffracted beams corresponding to either specular (0,0) or fractional order reflections are selected to yield bright-field (BF-LEEM) or dark-field (DF-LEEM) images, respectively. In LEEM, single-atom-height steps on the surface can be resolved by geometric phase contrast. Surface lateral resolution is typically of the order of a few tens of Ångstroms. Diffraction and chemical contrast also provide information about the surface. Since LEEM is not a scanning microscope, images are acquired at video rates, thus providing sufficient time resolution for real-time studies of dynamic phenomena such as epitaxy, interface formation, and surface morphological evolution on large lateral length scales (1-10 μm) over a wide range of temperatures. LEEM, best suited for investigating electrically conducting crystalline samples, has been used to study surface diffusion of 2D metal islands [28], surface phase transformations [29], alloy formation, step fluctuation kinetics, interlayer mass transport, and bulk diffusion. Photoelectron emission microscopy (PEEM) is a related technique, in which photoelectrons generated by an incident UV or an X-ray light source (rather than an electron gun) are used for imaging. PEEM has proven to be an effective tool for following chemical reactions on catalytic surfaces [30] and to study surface magnetism with elemental and/or chemical sensitivity [31].

There are several excellent review articles covering different aspects of atomic-scale dynamics of the early stages of thin film growth. Zinke-Allmang and co-workers [32,33] summarized the theoretical and experimental understanding of cluster formation phenomena in general, while focusing on the role of adatom surface diffusion and binding energies on cluster formation kinetics. Tromp and Hannon [34] described methods for quantitative analyses of nucleation and growth processes on surfaces. The reviews by Jeong and Williams [35] and Giesen [36] provide theoretical background and describe experimental and computational techniques for investigating and characterizing the dynamics of metastable structures on surfaces, determining step energetics and mass transport parameters, and hence developing an atomic-scale understanding of the stability of solid/vacuum and solid/liquid interfaces. Recently, Bonzel and co-workers [37,38] reviewed new experimental methods for analyses of temperature-dependent three-dimensional (3D) equilibrium crystal shapes and 2D islands as a means to extract absolute surface, step, and kink formation energies.

All of the above reviews focus on simple elemental metal and semiconductor surfaces. However, similar studies on more complex compound surfaces of technologically-relevant materials such as TiN, GaAs, GaN, ZnO, Al_2O_3, ZrO_2, have not been carried out. TiN, in particular, is widely used as a hard wear-resistant coating

on cutting tools, a diffusion-barrier layer in microelectronic devices, a corrosion-resistant coating on mechanical components, and an abrasion-resistant layer on optics and architectural glass. Since the elastic and diffusion-barrier properties of TiN are highly anisotropic, controlling polycrystalline TiN film texture is important for all of these applications. This fact has spurred interest in modeling the growth of polycrystalline TiN as a function of deposition conditions [39]. Such a model, however, requires knowledge of surface, step, and nearest-neighbor interaction energies, all as a function of orientation. Recently, considerable progress has been made toward obtaining absolute orientation-dependent step energies and step stiffnesses as well as the activation barriers for island coarsening on TiN(001) and TiN(111) surfaces [40].

Here, we describe recent progress toward elucidating the interplay of surface and bulk diffusion on morphological evolution of TiN(111) surfaces. Section III is a brief introduction to the phenomenon of Ostwald ripening and the coarsening/decay kinetics of 2D TiN islands on TiN(111) surfaces. Section IV deals with the interplay between surface and bulk diffusion processes and their role on surface step motion. In particular, section IV.A focuses on the effects of step permeability, step-step interactions, and bulk mass transport on the coarsening/decay of 3D island stacks. In section IV.B, we discuss the role of defects such as surface-terminated dislocations on step evolution kinetics.

II. EXPERIMENTAL PROCEDURE

Epitaxial TiN(111) layers, 2000-Å-thick, were grown on polished $Al_2O_3(0001)$ substrates at a temperature T = 1050 K in a load-locked multi-chamber ultra-high vacuum (UHV) system using magnetically-unbalanced dc magnetron sputter deposition [41] following the procedure described in Ref. 42.

The TiN(111) samples were then transferred to one of two UHV multichamber microscope systems, containing either a LEEM or a variable-temperature Omicron STM, and degassed at 1073 K for approximately 2 h. Each of the multichamber microscope systems has a base pressure $< 2x10^{-10}$ Torr and is equipped with facilities for sample preparation, residual gas analysis, electron-beam evaporation, ion sputtering, Auger electron spectroscopy, and low-energy electron diffraction (LEED). Sample temperatures were measured by optical pyrometry and calibrated using temperature-dependent TiN emissivity data obtained by spectroscopic ellipsometry.

In the following sections, we describe the evolution of ensembles of 2D adatom and vacancy islands on wide terraces, 3D stacks of 2D islands, and spiral surface steps. The adatom and vacancy islands were prepared by first depositing homoepitaxial TiN(111) buffer layers (50-100 Å thick) on the TiN(111) substrates described above at 1023 K by reactive evaporation from Ti rods (99.999% purity) in N_2 (99.999%) at $1x10^{-7}$ Torr. The buffer layers were annealed in N_2 for 4 h at a temperature T > 1100 K. Partial TiN(111) bilayers (BL)[1] with coverages of 0.1-0.8 BL were then deposited on the buffer layers by reactive-evaporation at room temperature. The samples were annealed *in situ* at T = 1050-1250 K in $1x10^{-7}$ Torr N_2 for times t = 1-2 h. The overall

---

[1] The [111] direction in B1-NaCl structure TiN is polar, consisting of alternating layers of Ti and N atoms.

procedure results in surfaces with $\simeq$ 500-Å-wide atomically-smooth terraces, separated by bilayer-height steps with triangular shaped (truncated hexagons) 2D TiN(111) adatom islands for coverages < 0.4 BL and vacancy islands at higher coverages [43].

Samples containing 3D mound structures on large (>1000 Å) terraces were prepared by depositing homoepitaxial TiN(111) overlayers (50-200 Å thick) at 1023 K and a rate of $\simeq$ 0.02 ML/s followed by annealing for 2-3 days in 5x10^{-8} Torr N$_2$ at 1200 K. The deposition/annealing cycles were repeated until 3D mounds, consisting of stacks of 2D TiN adatom islands appeared in defect-free areas and spiral structures were formed in the presence of surface-terminated dislocations [44,45].

Samples investigated by STM were allowed to thermally equilibrate with the tip at each annealing temperature for 2 to 3 h prior to obtaining images at a constant rate of 18 to 44 s/frame. Typical tunneling conditions were 0.4-0.6 nA at -3.5 V. Resolution in the images varied from 2 to 5 Å/pixel. Scan sizes, scan rates, and tunneling parameters were varied to check for tip induced effects. No such effects were observed for the results presented here. The samples studied by LEEM were allowed to thermally stabilize at each temperature for 10 to 15 s prior to acquiring LEEM videos at a rate of 30 frames/s. Typical imaging conditions were 4 μm field of view (corresponding to a resolution $\simeq$ 85 Å/pixel) and electron probe beam energies between 5 and 25 eV. Island boundaries were identified and the island areas determined during both STM and LEEM data analyses using the Image SXM [46] image processing software.

III.   OSTWALD RIPENING AND ISLAND DECAY

Ostwald ripening [47] is a phenomenon in which larger islands on a surface grow at the expense of smaller neighboring islands. Figs. 1a and 1b show representative STM images (1660x1660 Å^2) of 2D TiN(111) adatom and vacancy islands acquired at 34 s/frame during annealing at T = 1211 K for times t = 0 and 82 min, respectively. Most of the islands observed at t = 0 (e.g., adatom islands *1-6* and vacancy island *8*) have disappeared by t = 82 min, leaving only the largest island, labeled *7*.

Ostwald ripening is described by the Gibbs-Thomson equation [47] in which the equilibrium free adatom concentration ρ^{eq} associated with an island is related to the equilibrium island curvature κ through the expression

$$\rho^{eq} = \rho_\infty^{eq} \exp\left(\frac{\mu}{kT}\right), \tag{1}$$

where ρ_∞^{eq} is the equilibrium free adatom concentration associated with a straight step and μ is the island chemical potential. In the specific case of a circular (isotropic) island of radius r, the chemical potential is

$$\mu = \tilde{\beta}\kappa\Omega = \frac{\tilde{\beta}\Omega}{r}, \tag{2}$$

208

where $\widetilde{\beta}$ is the step stiffness, κ is the step curvature, and Ω is the unit molecular area. Smaller islands have higher curvatures and, hence, higher adatom concentrations than larger islands, resulting in mass transfer from smaller to larger islands.

The triangular shapes of the truncated hexagonal TiN(111) islands indicate that they are highly anisotropic, thus Eq. (2) is not applicable. The chemical potential associated with a non-circular (anisotropic) island shape is

$$\mu = \widetilde{\beta}(\varphi)\kappa(\theta)\Omega, \tag{3}$$

where κ and $\widetilde{\beta}$ are, respectively, functions of the azimuthal angle θ and the step normal φ. For an equilibrium-shaped island, the chemical potential per unit molecular area is independent of step orientation and depends only on island size, [42]

$$\lambda = \widetilde{\beta}(\varphi)\kappa(\theta) = \frac{B}{r_{avg}}. \tag{4}$$

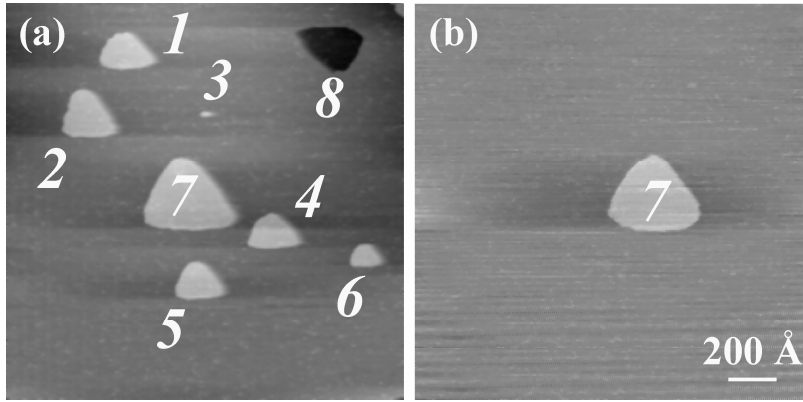**FIGURE 1.** Representative STM images (1660x1660 Å^2) of 2D TiN adatom (*1-7*) and vacancy islands (*8*) on an atomically-smooth TiN(111) terrace. The images were acquired at 34 s/frame at times t = (a) 0 and (b) 82 min during annealing at T = 1211 K.

In Eq. (4), $r_{avg} = (A/\pi)^{1/2}$ is the average island radius and B is an orientation-independent constant which sets the energy scale of the equilibrium island chemical potential. Substituting Eq. (4) into Eq. (1), the Gibbs-Thomson equation can be rewritten in terms of the *orientation-independent* parameters r_{avg} and B

$$\rho^{eq} = \rho^{eq}_{\infty} \exp\left(\frac{B\Omega}{r_{avg}kT}\right). \tag{5}$$

Eq. (5) is valid for any equilibrium island shape. For the case of circular islands, the step energy β is constant (orientation-independent), $B = \beta$, $r_{avg} = r$; and Eq. (5) reduces to the expression for the isotropic Gibbs-Thomson equation commonly found in the literature.

In classical mean-field theory, the decay rate dA/dt of an isotropic island exhibiting detachment-limited kinetics, which is the case for TiN(111) [43], is given by

$dA/dt = -K_d L\Omega[\rho^{eq} - \rho_s^{eq}]$ [48], where K_d is a temperature-dependent adatom attachment/detachment rate coefficient, L is the island perimeter, and ρ_s^{eq} is the equilibrium free adatom concentration on the surface. For an anisotropic island, where K_d may depend on step orientation, dA/dt is given by

$$\frac{dA}{dt} = -\Omega \int_0^{2\pi} d\theta\, r(\theta) K_d(\theta)\left[\rho^{eq} - \rho_s^{eq}\right]. \tag{6}$$

$r(\theta)$ in Eq. (6) is the radial distance from the island center to the edge as a function of θ. In the pure detachment-limited island coarsening regime, the case for TiN(111) islands [43], $\rho_s^{eq} = \rho_\infty^{eq}$ and assuming that the exponential term in Eq. (5) can be expanded to the first two terms[2], we obtain

$$\frac{dA}{dt} = -\Omega \rho_\infty^{eq} \int_0^{2\pi} d\theta\, r(\theta) K_d(\theta)\left(\frac{B\Omega}{r_{avg}kT}\right) = -\left(\frac{B\Omega^2 \rho_\infty^{eq}}{r_{avg}kT}\right) \int_0^{2\pi} d\theta\, r(\theta) K_d(\theta). \tag{7}$$

We note that Eq. (7), which shows that dA/dt is independent of island size for a given T in the detachment-limited regime, is valid even for anisotropic equilibrium-shaped islands.
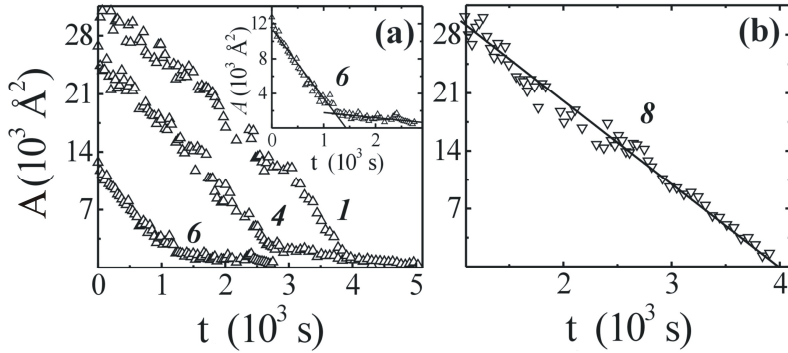

FIGURE 2. (a) Island area A vs. annealing time t for 2D adatom islands *1*, *4*, and *6* at T = 1211 K in Fig. 1a. A discontinuous decrease in decay rates was observed at a critical area A_c. Inset: A vs. t plot for island *6*. (b) A vs. t for vacancy island *8* in Fig. 1a. The solid lines in each case are linear least-squares fits to the data.

Typical results showing the areas A of adatom islands *1*, *4*, and *6* in Fig. 1a vs. t are plotted in Fig. 2a. The areas of all adatom islands were found to decrease linearly with t at a constant decay rate dA/dt, independent of local environment, with an abrupt decrease in slope at $A_c = 1600\pm470$ Å^2 (220±65 TiN molecules, $\Omega = 7.2$ Å^2), irrespective of both T and initial island area. This is illustrated more clearly for island *6* in the inset of Fig. 2a. dA/dt for island *6* decreases from 8.20 Å/s at $A > A_c$ to 1.28 Å/s at $A < A_c$. Measured dA/dt values for all adatom islands with $A > A_c$ were found

---

[2] For TiN(111), based on the stiffness and curvature values from Ref. [52], the maximum uncertainties introduced due to this assumption are $\simeq 0.1\%$ at A > Ac and $\simeq 2.5\%$ at A < Ac.

to be a factor of 3 to 20, depending monotonically on T, higher than the same islands with $A < A_c$.

Fig. 2b is a plot of A vs. t for the vacancy island 8 in Fig. 1a. dA/dt remains constant, with no slope transition, over the entire decay process. A vs. t data in Figs. 2a and 2b are typical of STM results obtained from over 80 large ($A > A_c$) and 40 small ($A < A_c$) adatom islands and 5 vacancy islands observed at temperatures in the range 1050-1250 K.

dA/dt, in Eq. (7), is a function of the product of the thermally-activated parameters ρ_∞^{eq} and K_d. Thus, dA/dt can be expressed in the form $dA/dt \propto \exp(E_a/kT)$ with an activation barrier E_a. From an Arrhenius plot of the island decay rates, we obtain an activation energy $E_{ad,small} = 3.3\pm0.4$ eV for small ($A < A_c$) adatom islands and $E_{ad,large} = 2.3\pm0.6$ eV for large ($A > A_c$) adatom islands. The activation energy for decay of vacancy islands is $E_{vac} \lesssim E_{ad,large}$.

In the detachment-limited regime, $E_a = E_f + E_s + E_d$, where E_f, E_s, and E_d are the adatom formation energy, surface diffusion barrier, and attachment/detachment barrier, respectively. Since E_f and E_s are independent of island size, ($E_{ad,small} - E_{ad,large}$) corresponds to a difference in E_d values for small and large adatom islands. It is reasonable to assume, based upon direct observations [49,50], that at relatively low temperatures, which is the case here where T varies from 0.33 to 0.39 of the TiN melting point in K [51], attachment/detachment occurs only at kink sites. Thus K_d, and hence E_d, depend on the kink density (number of kinks per unit step length), which in turn depends on the kink formation energy ε. For TiN(111), $\varepsilon_1 \simeq 0.43$ eV and $\varepsilon_2 \simeq 0.13$ eV, where ε_1 and ε_2 correspond to kink formation energies along S_1 (long steps, "triangle" sides) and S_2 (short steps, rounded corners) respectively [52]. Thus, for large islands, attachment/detachment of diffusing species occurs preferentially along S_2 steps. Islands with $A \leq A_c$ ($A_c = 1600$ Å^2) are bounded by S_2 steps of length ≤ 4 atoms and S_1 steps of length ≤ 12 atoms. Kink formation along 4-atom-long S_2 steps involves removal of an atom to produce a double kink, which is energetically unfavorable. Thus, for islands with $A \leq A_c$, attachment/detachment of diffusing species occurs predominantly along S_1 steps which have higher kink formation energies and, hence, higher E_{ad} values and lower decay rates as we observe. In the case of vacancy islands, E_{vac} and, hence, E_d are independent of island size suggesting different pathways for attachment/detachment at adatom and vacancy islands.

IV. EFFECTS OF BULK DIFFUSION ON SURFACE EVOLUTION KINETICS

In the previous section, we showed that a detachment-limited surface diffusion mechanism, driven by the Gibbs-Thomson effect, is sufficient to explain the coarsening/decay kinetics of both adatom and vacancy islands on TiN(111) surfaces. However, other effects such as bulk diffusion and interlayer mass transport can also affect surface morphological evolution kinetics, and even become dominant at higher temperatures. In the following sections, we describe two step-flow models, developed

211

based upon the Burton-Cabrera-Frank (BCF) theory of crystal growth [53], that account for step-step interactions, step permeability, and both surface and bulk mass transport processes.

IV.A. 3D-Mound Decay: Effects of Bulk Diffusion and Step Permeability

The coarsening/decay behavior of 3D mounds consisting of 2D layer structures in a "wedding cake" configuration has been studied extensively, both experimentally [54-56] and theoretically [57-59]. Experimental studies of the coarsening/decay kinetics of 2D homoepitaxial semiconductor and fcc metal islands stacked in 3D mound geometries indicate that the rate-limiting processes controlling island decay behavior are both qualitatively and quantitatively different from those of isolated islands on terraces [54,55,60-62]. In this section, we describe the coarsening/decay kinetics of concentrically-stacked 2D TiN adatom islands on TiN(111) terraces at elevated temperatures (T = 1550-1700 K). The islands exhibit repulsive step-step interactions and high step permeability rates.

Fig. 3a is a typical BF-LEEM image acquired during annealing a TiN(111) sample at T = 1559 K. We follow the time- and temperature-dependent decay kinetics of several successive layers in the circled region shown at higher magnification in Fig. 3b. This simple configuration allows us to apply the step flow model, developed by Israeli and Kandel [59]. The model is based upon the BCF theory of crystal growth [53] and accounts for the effects of step-step interactions, step permeability, and both surface and bulk mass transport on surface step motion.

The ith island of area A_i in a given 3D mound is characterized by its average radius r_i (i is a running index which increases from the top of the mound to the bottom.) In the absence of net mass change due to deposition, evaporation, and/or bulk diffusion, the adatom concentration fields between the islands are described by the 2D steady-state diffusion equation

$$\nabla^2 \rho_i(r) = 0, \text{ with } r_{i-1} \leq r \leq r_i , \tag{8}$$

where $\rho_i(r)$ is the adatom concentration on the ith terrace. A steady-state solution is justified since the time scales associated with equilibration of adatom concentration fluctuations on the terraces are much shorter than those associated with island step motion. We solve Eq. (8) using boundary conditions (given below) which specify adatom fluxes into (or out of) the islands and, hence, determine the rate of change of island radii. Assuming first-order kinetics, the flux boundary conditions at the ith island are

$$D_s \left.\frac{\partial \rho_i}{\partial r}\right|_{r_i} = K_d \left(\rho_i|_{r_i} - \rho_i^{eq}\right) + p\left(\rho_i|_{r_i} - \rho_{i-1}|_{r_i}\right),$$

$$D_s \left.\frac{\partial \rho_{i-1}}{\partial r}\right|_{r_i} = -K_d \left(\rho_{i-1}|_{r_i} - \rho_i^{eq}\right) + p\left(\rho_i|_{r_i} - \rho_{i-1}|_{r_i}\right). \tag{9}$$

In Eq. (9), D_s is the surface diffusivity, K_d is the attachment/detachment rate, and p is the step permeability. ρ_i^{eq} is the equilibrium adatom concentration in the vicinity of

212

the ith step, which is related to the step chemical potential μ_i and the equilibrium adatom concentration ρ_∞^{eq} at a straight isolated step through the Gibbs-Thomson relation, Eq. (1).

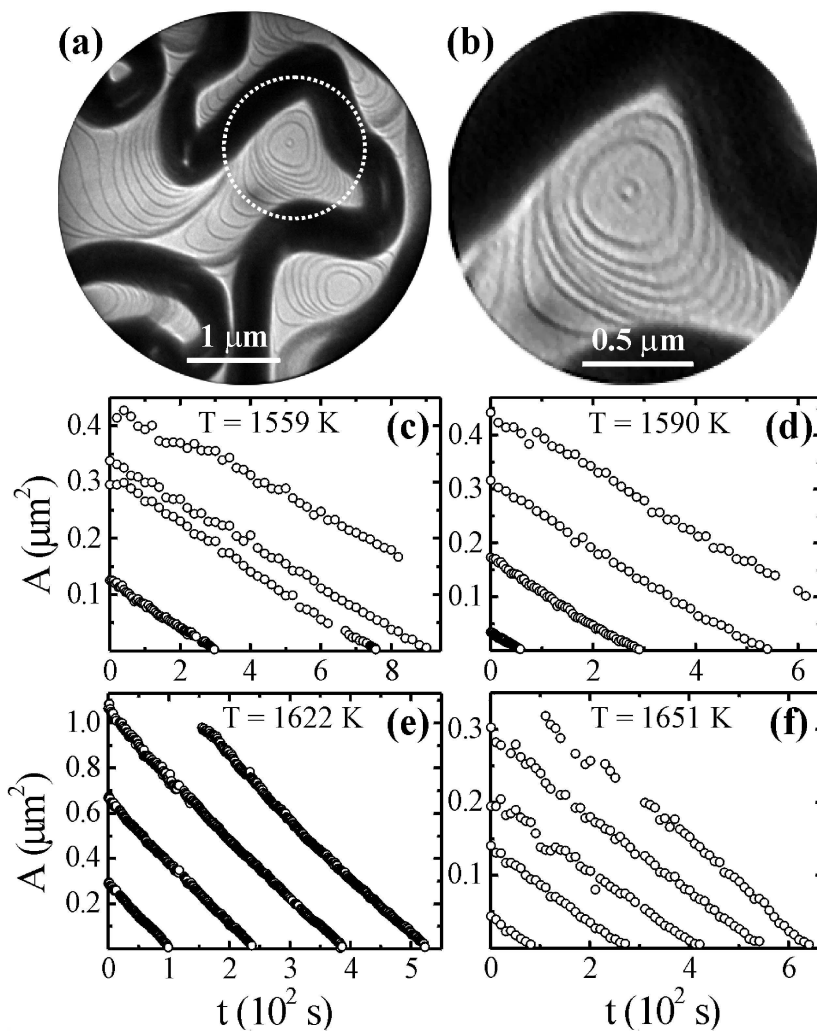**FIGURE 3.** (a) Typical BF-LEEM image (field of view = 4.0 μm; E = 13 eV) of a 3D conical stack of 2D homoepitaxial islands on TiN(111) during annealing at T = 1559 K. (b) Higher-resolution image (field of view = 1.7 μm) of the highlighted region in Fig. 3a. (c)-(f): island area A vs. annealing time t plots for four or more successive layers in the region highlighted in Fig. 3b at temperatures T of (c) 1559 K, (d) 1590 K, (e) 1622 K, and (f) 1651 K.

For an island in a stack, μ_i depends on the island curvature and on elastic and entropic repulsive interactions between nearest-neighbor steps, accounting for which yields the relationship[3] [35,54,59]

$$\mu_i = \frac{\Omega B}{r_i} + \Omega G \left(\frac{2r_{i+1}}{(r_{i+1}+r_i)(r_{i+1}-r_i)^3} - \frac{2r_{i-1}}{(r_i+r_{i-1})(r_i-r_{i-1})^3} \right), \qquad (10)$$

where G is the step-step repulsive interaction strength.

Expanding the exponential term in the Gibbs-Thomson equation to the first two terms, as in Eq. (7), and solving Eq (8) for ρ_i with the boundary conditions specified by Eqs. (9) and (10), yields the rate of change dr_i/dt of each island radius. For the limiting case in which the steps are impermeable, i.e. $p = 0$, and there is no bulk mass transport, we obtain

$$\frac{dr_i}{dt} = \frac{\Omega K_d \rho_\infty^{eq}}{r_i \, kT} \left[\frac{\mu_i - \mu_{i+1}}{\frac{K_d}{D_s}\ln\left(\frac{r_i}{r_{i+1}}\right) - \left(\frac{1}{r_i}+\frac{1}{r_{i+1}}\right)} - \frac{\mu_{i-1}-\mu_i}{\frac{K_d}{D_s}\ln\left(\frac{r_{i-1}}{r_i}\right) - \left(\frac{1}{r_{i-1}}+\frac{1}{r_i}\right)} \right]. \qquad (11)$$

If the steps are permeable ($p > 0$), however, adatoms can hop across without becoming incorporated at the step edges and mass is not conserved locally. This results in coupling of the adatom diffusion fields on all terraces. Consequently, the equations describing the areal rate of change for the ith island are linked with those describing each of the other islands in the stack and we must solve the full equation set.

Adatom transport between the bulk and the surface also leads to local non-conservation of mass. In order to account for this possibility, we follow Ref. [56] and assume that mass exchange with the bulk occurs only near island edges at a rate K_{bulk}. The adatom flux J_i from the ith step to the bulk is then given by

$$J_i = K_{bulk}\left(\frac{\rho_\infty^{eq}}{kT}\right)\mu_i, \qquad (12)$$

where we make the assumption that the bulk chemical potential is at equilibrium. Combining Eqs. (11) and (12), we obtain an expression for the velocity dr_i/dt of impermeable steps ($p = 0$) in the presence of bulk diffusion,

$$\frac{dr_i}{dt} = \frac{\Omega K_d \rho_\infty^{eq}}{kT \cdot r_i}\left[\frac{\mu_i - \mu_{i+1}}{\frac{K_d}{D_s}\ln\left(\frac{r_i}{r_{i+1}}\right) - \left(\frac{1}{r_i}+\frac{1}{r_{i+1}}\right)} - \frac{\mu_{i-1}-\mu_i}{\frac{K_d}{D_s}\ln\left(\frac{r_{i-1}}{r_i}\right) - \left(\frac{1}{r_{i-1}}+\frac{1}{r_i}\right)} - K_{bulk}\cdot r_i \cdot \mu_i \right]. \qquad (13)$$

The step-flow model outlined above contains several material parameters: Ω, D_s, K_d, K_{bulk}, p, ρ_∞^{eq}, B, and G, of which only Ω ($=7.2$ Å^2) and B ($= 0.23 \pm 0.01$ eV/Å) are known for TiN(111) [63]. There are four independent variables which control island

---

[3] In deriving Eq. (10), we assume circular-shaped islands that are concentrically stacked and separated by a distance that is smaller than the island radii.

214

decay kinetics. The length scale $l = \dfrac{D_s}{K_d}$ defines the limiting surface mass transport mechanism. In the diffusion-limited island coarsening regime, $l \ll \Delta x$, where Δx is the average terrace width, while $l \gg \Delta x$ in the detachment-limited regime. The ratios $\dfrac{p}{K_d}$ and $\dfrac{K_{bulk}}{K_d}$ describe the relative importance of step permeability and surface mass exchange with the bulk, respectively. Finally, the dimensionless quantity $g = \left(\dfrac{kT}{\Omega}\right)^2 \dfrac{G}{B^3}$ is a measure of the step-step interaction strength G. ρ_∞^{eq}, the only term not included in these four parameters, affects only the time scale of step motion and can easily be accounted for by rescaling the time unit.
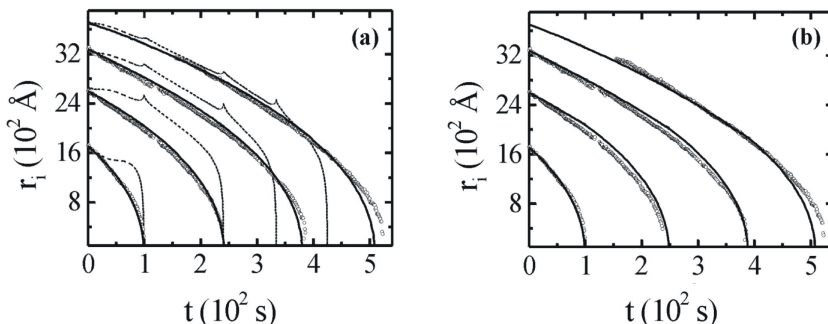

FIGURE 4. (a), (b): Plots of island radii r_i vs. annealing time t at T = 1622 K for the four samples corresponding to the data in Fig. 3e. The dashed and solid lines in Figs. 4a and 4b are calculated curves describing the LEEM data (open circles). The dashed lines in Fig. 4a are obtained assuming that the steps are impermeable and that there is no net bulk mass transport, i.e. $p = K_{bulk} = 0$. The solid lines in Figs. 4a and 4b are obtained assuming permeable steps ($p > 0$) with no bulk mass transport ($K_{bulk} = 0$) and bulk transport ($K_{bulk} > 0$) with impermeable steps ($p = 0$), respectively.

Fig. 4 shows a typical example of the agreement between experimental results at T = 1622 K and model predictions. The open circles in Figs. 4a and 4b are measured TiN(111) island radii as a function of time. The dashed lines in Fig. 4a are best fit calculated curves, obtained under the constraint of local mass conservation, i.e. $p = 0$ and $K_{bulk} = 0$, with $D_s/K_d = 0.1$ μm and $g = 0.0631$, for each island. While this relatively strong step-step interaction tends to minimize the recoil (the spike in lower island radii observed at times corresponding to the complete disappearance of the top island), the quality of the fits are far from satisfactory. Thus, as expected, imposing complete local mass conservation cannot explain the observed results, which require the presence of highly permeable steps and/or bulk mass transport.

The solid lines in Figs. 4a and 4b are calculated best fit solutions obtained by relaxing the local mass conservation constraint. We allow step permeability ($p > 0$) in the absence of bulk mass transport ($K_{bulk} = 0$) in Fig. 4a and bulk transport $K_{bulk} > 0$ with impermeable steps ($p = 0$) in Fig. 4b. For the first case, the best fit parameter values are $D_s/K_d = 100$ μm, $p/K_d = 2000$, and $g = 0.00819$, indicative of detachment-

215

limited decay kinetics with highly permeable steps. In the second case, we obtain $D_s/K_d = 0.5$ μm, $K_{bulk}/K_d = 2.5$, and $g = 0.00354$. It is important to note that calculated curves obtained with bulk diffusion as the sole mass transport mechanism, e.g. with $D_s = 0$, are not consistent with the experimental results at any annealing temperature, $T = 1550$-1700 K, suggesting that the observed decay of TiN(111) islands requires the presence of surface mass transport.

TABLE 1.A. Permeable steps ($K_{bulk} = 0$)

T	D_s/K_d (μm)	p/K_d	G	G (eV-Å)
1559 K	100	2000	9.78×10^{-4}	0.034
1590 K	200	2000	2.82×10^{-3}	0.095
1622 K	100	2000	8.19×10^{-3}	0.264
1651 K	200	2000	2.45×10^{-2}	0.7634

TABLE 1.B. Bulk exchange (p=0)

T	D_s/K_d (μm)	p/K_d	G	G (eV-Å)
1559 K	5	2	1.02×10^{-3}	0.036
1590 K	0.5	10	$< 10^{-5}$	$< 3.4 \times 10^{-4}$
1622 K	0.5	2.5	3.54×10^{-3}	0.114
1651 K	0.5	5.5	2.31×10^{-2}	0.7198

Table 1 summarizes the materials parameters used to obtain the best fit solutions to the experimental data acquired at all four annealing temperatures in the two limits for which mass is not conserved locally: step permeability and bulk mass transport. Excluding bulk diffusion leads to high step permeabilities with D_s/K_d values which are much larger than the average terrace width (~ 1000 Å). This is a signature of detachment-limited kinetics and, as such, is in agreement with previous high-temperature ($T = 1000$-1250 K) scanning tunneling microscopy (STM) measurements of 2D TiN island coarsening/decay kinetics on TiN(111) terraces [43]. If we include bulk mass transport with impermeable steps, we obtain K_{bulk}/K_d ratios of order unity except at $T = 1590$ K, where $K_{bulk}/K_d = 10$. The calculated D_s/K_d values in Table 1.B also correspond to detachment-limited kinetics, but they are significantly smaller than the results obtained for permeable steps. This large difference in D_s/K_d values can be understood as follows. Step permeability by itself does not facilitate mass transport. It must be accompanied by fast surface diffusion in order to significantly violate local mass conservation. For bulk diffusion, this is not the case and mass is not conserved locally even with a modest value of D_s/K_d.

Overall, we find that the agreement between the experimental data and the calculated results obtained with non-zero K_{bulk} values is better than that obtained with high p/K_d values. However, the differences are small and we cannot quantitatively distinguish between the two processes. Since step permeability, unlike bulk-diffusion, is a surface process and given that bulk-point defects usually have larger formation and diffusion energies than surface adspecies, the energetics controlling island decay should provide additional insights into the controlling mechanism. To this purpose, we measured island decay rates as a function of temperature for 23 islands at four different temperatures between 1550 and 1700 K [44]. From least-squares analyses of the results, we obtain an activation energy E_d of 2.8 ± 0.3 eV for the decay kinetics of 2D TiN(111) islands stacked in 3D mounds. This is consistent with the previously

216

reported value of 2.3 ± 0.6 eV determined from STM observations of the decay of large 2D TiN(111) islands on atomically-flat terraces [43]. The fact that we obtain an E_d value which is significantly lower than the bulk-mass transport barrier, 4.5±0.2 eV, measured for TiN(111) spiral step growth [64] provides further evidence that the dominant mass transport mechanism is surface, rather than, bulk diffusion. Thus, we attribute the decay of 2D TiN(111) islands in 3D concentric mound structures primarily to the presence of highly permeable steps in the detachment-limited regime.

IV.B. Bulk Diffusion and Surface Spiral Steps

In this section, we focus on the dynamics of surface loops and spiral steps, arising from the surface termination of a screw dislocation. Despite the fact that dislocations terminating on surfaces can strongly influence nanostructure stability, mechanical properties of thin films, chemical reactions, transport phenomena, and other surface processes; most theoretical and experimental studies have focused on dislocation motion in bulk solids under applied stress [65,66] and step formation due to dislocations at surfaces during crystal growth [25,26,53,67] or evaporation [68,69,70]. As a result, very little is known concerning the near-equilibrium dynamics of dislocations at surfaces.
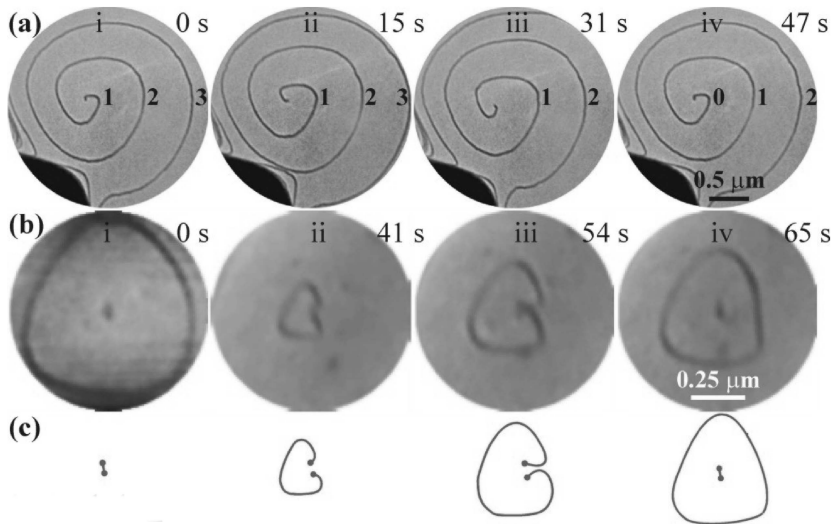

FIGURE 5. LEEM images showing nucleation and growth of bilayer-height surface steps at the cores of dislocations terminating on TiN(111) terraces during annealing in N_2 at temperatures T. The images were acquired as a function of time t. The dark lines in the LEEM images are ⟨110⟩-oriented bilayer-height steps (the [111] direction in B1-NaCl structure TiN is polar, consisting of alternating layers of Ti and N atoms). (a) Field of view ≈ 2.53 µm; T = 1688 K. Spiral steps form due to the pinning of a step edge at a dislocation core. (b) Field of view ≈ 0.93 µm; T = 1653 K. Loops nucleate and grow centered around a step edge pinned at both ends by dislocations of opposite sign. (c) Schematic diagram of the loop generation process observed in (b).

217

Figures 5a and b illustrate the nucleation and growth of TiN(111) spiral steps and loops at the cores of dislocations terminating on TiN(111) surfaces as observed in-situ by LEEM [71] during annealing in N_2. (We define a loop as a 2D island formed around a surface step segment pinned at both ends by dislocations). Fig. 5a shows the formation of a concentric spiral step structure around a dislocation core, while the images in Fig. 5b capture the nucleation and growth of a closed loop. The spiral and loop steps both exhibit three-fold symmetry with a truncated-hexagonal shape, i.e. the near-equilibrium shape of 2D TiN(111) islands [52], indicative of fast step edge diffusion. Note that these spirals and loops are observed during annealing with no net mass gain or loss and, as we will show, are *not* the growth structures predicted by BCF [53].

Figures 5a i-iv reveal a remarkable feature: the spiral steps rotate around the dislocation core resulting in an increase in the total step length with time t as the spirals undergo a shape-preserving anticlockwise motion with a constant angular velocity ω. That is, the shape and size of the spiral are periodic with time $\tau = 2\pi/\omega$. For the spiral shown in Figs. 5a i-iv, $\tau = 47$ s corresponds to one complete rotation at the annealing temperature $T = 1688$ K; the spiral shown in i is geometrically identical to the one in iv. During the period τ, the layer labeled 3 disappears from the field of view in Fig. 5a iii and a new layer, labeled 0, is formed (Fig. 5a iv) as the dislocation core climbs by a unit step height, $a_\perp = 2.4$ Å, normal to the surface.

Figs. 5b i-iii show nucleation and growth of a loop originating at a defect. Upon detaching from the defect, the expanding loop (Fig. 5b iv) regains the equilibrium shape of 2D TiN(111) islands [52]. This process, like the nucleation and growth of spiral steps, is also periodic. For the loops shown in Figs. 5b i-iv, $\tau = 85\pm5$ s corresponds to the loop nucleation period at $T = 1653$ K.

Analogous to the growth spirals and loops observed in bulk solids due to the operation of Frank-Read [72] and/or Bardeen-Herring [73] sources under applied stress [74], and on surfaces during crystal growth as predicted by the BCF theory [53], the features observed in Figs. 5a and b are due to surface steps pinned by a single dislocation (in the case of a spiral) and a pair of oppositely signed dislocations (for a loop), respectively. For a single dislocation, the steps emanating from the cores wind into expanding spirals. With a pair of oppositely signed dislocations, as illustrated in the schematic diagrams of Fig. 5c, the expanding spirals originating from the cores rotate in opposing directions, eventually coming into contact to form a loop which increases in size.

Our model for this phenomenon is based upon two assumptions. (1) A non-equilibrium concentration of point defects exists in the bulk. This is reasonable based upon the fact that TiN_x is known to have a very wide single phase region extending from x = 0.6 to x = 1.2 and can sustain both high anion (N) and cation (Ti) vacancy concentrations [75]. Given that we observe steps emanating from the grooves (the thick dark lines visible in the LEEM images in Fig. 5) annihilating the spiral steps, we conclude that spirals grow inward, normal to the surface. Note, however, that there is no net mass gain or loss. The surface point defect concentration C_s^{eq} is at thermal equilibrium since a N-terminated surface is energetically favourable for TiN(111) [76]. (2) Dislocation cores emit/absorb point defects at a thermally activated time-

218

independent rate R; a plausible assumption given that dislocation cores act as sources/sinks for point defects [77,78].

Consider, for simplicity, a circular loop of radius r_{loop} centered around a core region of finite radius r_{core}. The surface point defect concentration $C(r)$ at any position r, with $r_{core} < r < r_{loop}$, is given by the diffusion equation $\partial C(r)/\partial t = D_s \nabla^2 C(r)$, where D_s is the surface diffusivity. Within the quasistatic approximation, i.e. surface diffusion is much faster than the step edge velocity, $\partial C(r)/\partial t = 0$. The general solution of the resulting Laplace equation $\nabla^2 C(r) = 0$ is $C(r) = C_1 \ln(r) + C_2$, where the constants C_1 and C_2 are determined by the boundary conditions at the core and the loop. From assumption (2) above, the flux $-D_s \nabla C(r)$ of point defects at the core is

$$-D_s \nabla C(r)\big|_{r\,=\,r_{core}} = \frac{R}{2\pi r_{core}}, \tag{14}$$

while at the loop:

$$-D_s \nabla C(r)\big|_{r\,=\,r_{loop}} = k_s[C(r_{loop}) - C_{loop}^{eq}]. \tag{15}$$

In Eq. (15), k_s is the rate of attachment/detachment at the step and $C_{loop}^{eq} = C_s^{eq}\exp\left(\mu_{loop}/k_B T\right)$, from the Gibbs-Thomson relation (1), is the equilibrium point defect concentration due to the curvature-dependent chemical potential μ_{loop} associated with the loop. Solving for C_1 and C_2 yields the normal component of the loop velocity dr_{loop}/dt as

$$\frac{dr_{loop}}{dt} = \Omega k_s[C(r_{loop}) - C_{loop}^{eq}] = \frac{\Omega}{2\pi r_{loop}} R. \tag{16}$$

In deriving the above formalism, we have neglected the curvature-driven flux from the loop to the local environment. In the detachment-limited regime, the contribution to dr_{loop}/dt due to this flux, which is proportional to $-1/r_{loop}$, is small and hence will have little effect on the growth velocity dr_{loop}/dt in Eq. (16). The important point is that the form of Eq. (16) is qualitatively different from Eq. (7), the parallel equation describing the 2D island decay (Ostwald ripening) process. We note that Eq. (16) is also valid, without loss of generality, for non-circular loops and spiral steps far from the core. Clearly, from Eq. (16), the loop (and spiral) growth rate $dA/dt = \Omega R$ is time-invariant consistent with the constant slopes obtained in our measurements of A vs. t in Fig. 6.

In formulating Eq. (16), we assume an equilibrium defect concentration C_{loop}^{eq} associated with the loop. This is justified for the first loop, since steps near the core and far from the boundary maintain a truncated-hexagonal shape with 3-fold symmetry, the equilibrium shape of TiN(111) islands. (This observation also suggests that localized growth flux at the cores may have negligible effect on step shapes.) However, far from the cores we find: (i) steps with non-equilibrium shapes that vary with the spiral geometry and (ii) step bunching. We attribute these observations to the presence of grooves bounding the spirals. Hence, modelling growth kinetics of multiple loop/spiral steps requires a better understanding of the effects of the geometric constraints imposed by physical boundaries on step chemical potentials
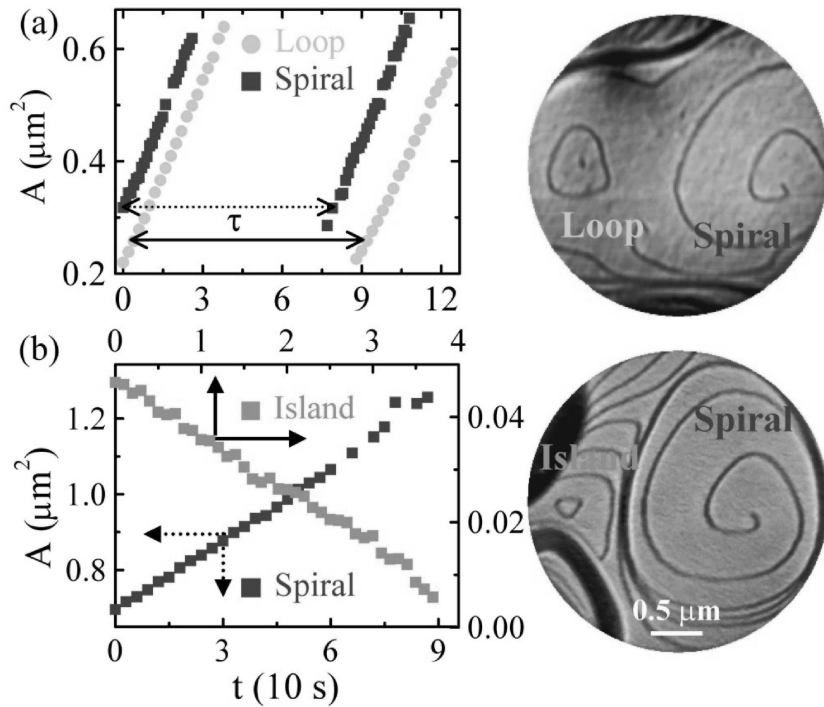
FIGURE 6. Area vs. annealing time for 2D TiN loops, spirals, and islands on TiN(111). (a) Time-dependent areas A of 2D TiN loops and spirals on a TiN(111) surface (shown in the image to the right) during annealing at T = 1653 K. (We only measure areas of loops that formed upon detaching from the central core and have attained near-equilibrium truncated-hexagonal shapes as in Fig. 5b iv). Spiral areas are calculated as $A(t) = \frac{1}{2} \int_{\pi}^{3\pi} [r(\theta, t)]^2 \, d\theta$. The spiral shape function r(θ,t) is defined for θ in the range 0 to ∞, and $\pi \leq \theta \leq 3\pi$ corresponds to an outwardly moving spiral step segment, far from the core, which area increases linearly with time. τ is the average time required to generate successive spirals and loops that have the same area. (b) The time-dependent areas A of spirals and 2D TiN islands on TiN(111) terraces (shown in the image to the right) during annealing at T = 1694 K. Note that the left and bottom axes of the plot correspond to that of the spiral while the right and top axes correspond to the island. The spiral area increases linearly with time while the island area decreases. The fields of view in both images are ≈ 2.75 μm.

Finally, our model assumes a constant rate R for the emission/absorption of point defects at dislocation cores. R depends on two driving forces: (1) minimization of dislocation line energy and (2) equilibration of bulk point defects. In the first case, spiral and loop growth will continue to occur until the disappearance of the dislocation core. In the second case, however, R is a function of the concentration gradient between the surface and the bulk, which decreases with time. Hence, this driving force terminates upon equilibration of the bulk point defect concentration.
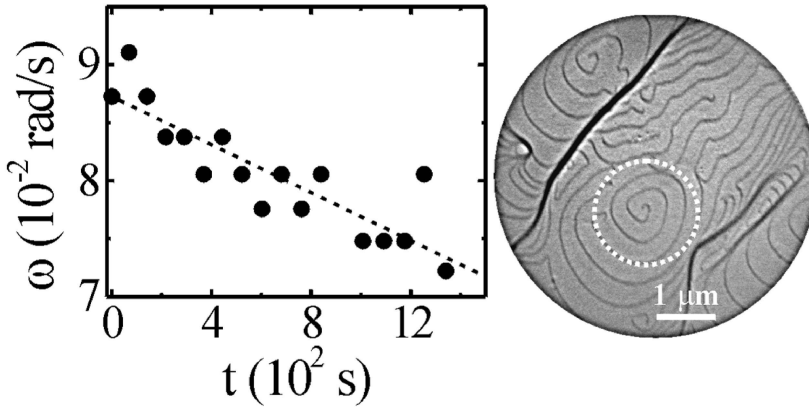
FIGURE 7. ω vs. t plot for successive spiral steps in the region highlighted in the associated LEEM image (field of view = 5.6 μm). The data were acquired during annealing a TiN(111) sample at T = 1727 K with $p_{N_2} = 5\times10^{-8}$ Torr. The dashed line is a linear least-squares fit to the measured data.

In order to test the validity of our model, we studied the long time behavior of spiral growth rates. Fig. 7 is a typical plot of ω vs. t values (solid circles) obtained from 17 successive spirals generated from the same dislocation core (highlighted in the associated LEEM image) while annealing a TiN(111) sample at T = 1727 K with p_{N_2} held constant at 5×10^{-8} Torr. We find that ω decreases monotonically from $\simeq$ 0.09 rad/s to $\simeq$ 0.07 rad/s, i.e. an $\simeq$22% reduction in ω, within 1340 s at 1727 K. If we assume a linear relationship, the $\omega(t)$ data can be fit using least-squares analyses (dashed line in Fig. 7). The observed decrease in ω with time can be attributed to: (1) the effect of already existing steps on the nucleation of new steps (a "back-force" effect [79]) and/or (2) equilibration of the point-defect concentration in the bulk. In the first case, the geometry of the spiral structures, while in the second case, the N_2 pressure, could affect the TiN(111) spiral step growth kinetics. Since the spirals in our experiments are situated in very similar surface geometries, the effect of local environment on spiral growth kinetics cannot be determined. Thus, we focused on the effects of p_{N_2}.

We measured ω while varying p_{N_2} between zero and 5×10^{-7} Torr at constant T. Fig. 8 contains typical plots of ω (solid circles) and dA/dt (open squares) as a function of t at T = 1670 K. p_{N_2}, set initially to 5×10^{-8} Torr, is suddenly reduced to zero ($\leq$ 5×10^{-9} Torr) at t = 390 s and then varied between zero and 5×10^{-7} Torr. ω and dA/dt, while exhibiting an overall decrease with time, do not vary systematically with p_{N_2}; suggesting that molecular N_2 does not significantly change the surface and bulk compositions of N-terminated TiN(111).

From an Arrhenius plot of $\omega(T)$ data, determined from separate sets of LEEM images acquired at four different temperatures T, we find an activation energy E_d = 4.5±0.2 eV; compared to 2.3±0.6 eV for the decay of 2D TiN islands on TiN(111).

221

The fact that we measure a higher activation barrier E_d for spiral growth than for island decay (and E_d is significantly lower than the desorption energies for TiN and Ti adspecies [76]) provides strong evidence that the dominant mass transport is along dislocation lines rather than surface diffusion or evaporation. Hence, E_d corresponds to the activation barrier for dislocation motion which is generally associated with point defect formation and migration along the dislocation (also referred to as "pipe diffusion") [80]. This is physically reasonable since bulk point defect migration, expected to influence surface dynamics at sufficiently high temperatures [56], has a smaller activation barrier along dislocation lines [80] than in dislocation-free areas.
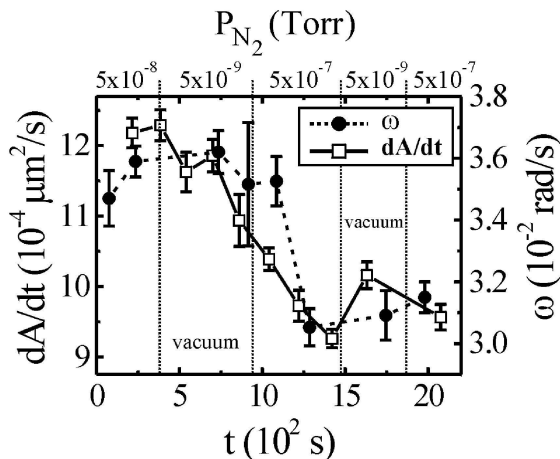

FIGURE 8. Plots of dA/dt (open squares) and ω (solid circles) vs. t for 2D TiN(111) islands during annealing at T = 1670 K while varying p_{N_2} between zero and 5×10^{-7} Torr as shown.

V. CONCLUSIONS

In this chapter, we discuss recent progress toward developing a fundamental understanding of morphological evolution on surfaces of compounds such as TiN. In situ high-temperature STM and LEEM studies provide insights into the effects of surface- and bulk-mass transport processes on surface step motion. Specifically, we focused on the effects of step permeability, step-step interactions, bulk diffusion, and surface-terminated dislocations on the coarsening/decay kinetics of 3D island stacks; and the dynamics of surface steps.

This report is intended to complement and extend the existing literature on both isotropic and anisotropic island dynamics. With the recent surge of interest in synthesis and characterization of nanostructures, there is growing need for understanding the atomic-scale mechanisms governing the formation and stability of nanostructures. Our studies are an effort to extend the existing formalism describing 2D island dynamics to the analyses of surface defects and anisotropic 3D nanostructures.

ACKNOWLEDGEMENTS

REFERENCES

1. G. Binnig, H. Rohrer, C. Gerber, *Appl. Phys. Lett.* **40**, 178 (1982).
2. G. Binnig, C.F. Quate, C. Gerber, *Phys. Rev. Lett.* **56**, 930 (1986).
3. E.W. Müller, *Z. Phys.* **131**, 136 (1951).
4. S.C. Wang and G. Ehrlich, *Phys. Rev. Lett.* **79**, 4234 (1997).
5. S. C. Wang, U. Kürpick, and G. Ehrlich, *Phys. Rev. Lett.* **81**, 4923 (1998).
6. G. Ehrlich, *Surf. Sci.* **331-333**, 865 (1995) and references therein.
7. F. Besenbacher, P.T. Sprunger, L. Ruan, L. Olesen, I. Stensgaard and E. Lægsgaard, *Topics in Catalysis* **1**, 325 (1994).
8. L. Petersen, M. Schunack, B. Schaefer, T.R. Linderoth, P.B. Rasmussen, P.T. Sprunger, E. Lægsgaard, I. Stensgaard and F. Besenbacher, *Rev. Sci. Instr.* **72**, 1438 (2001).
9. E. Lægsgaard, L. Österlund, P. Thostrup, P.B. Rasmussen, I. Stensgaard, and F. Besenbacher, *Rev. Sci. Instr.* **72**, 3537 (2001).
10. K. Morgenstern, *Phys. Stat. Sol. (b)* **242**, 773 (2005).
11. M.J. Rost, L. Crama, P. Schakel, E. van Tol, G.B.E.M. van Velzen-Williams, C.F. Overgauw, H. ter Horst, H. Dekker, B. Okhuijsen, M. Seynen, A. Vijftigschild, P. Han, A. J. Katan, K. Schoots, R. Schumm, W. van Loo, T. H. Oosterkamp, and J.W.M. Frenken, *Rev. Sci. Instr.* **76**, 053710 (2005).
12. J. de la Figuera, J. E. Prieto, C. Ocal, and R. Miranda, *Solid State Communications* **89**, 815 (1994).
13. J.-M. Wen, S.-L. Chang, J.W. Burnett, J.W. Evans, and P.A. Thiel, *Phys. Rev. Lett.* **73**, 2591 (1994).
14. K. Morgenstern, G. Rosenfeld, B. Poelsema, and G. Comsa, *Phys. Rev. Lett.* **74**, 2058 (1995).
15. J.-M. Wen, J.W. Evans, M.C. Bartelt, J.W. Burnett, and P.A. Thiel, *Phys. Rev. Lett.* **76**, 652 (1996).
16. C.R. Stoldt, C.J. Jenks, P.A. Thiel, A.M. Cadilhe, and J.W. Evans, *J. Chem. Phys.* **111**, 5157 (1999).
17. W.W. Pai, A.K. Swan, Z. Zhang, and J.F. Wendelken, *Phys. Rev. Lett.* **79**, 3210 (1997).
18. T. R. Linderoth, S. Horch, L. Petersen, S. Helveg, E. Lægsgaard, I. Stensgaard, and F. Besenbacher, *Phys. Rev. Lett.* **82**, 1494 (1999).
19. K. Morgenstern, E. Lægsgaard, and F. Besenbacher, *Phys. Rev. Lett.* **86**, 5739 (2001).
20. K. Morgenstern, E. Lægsgaard, and F. Besenbacher, *Phys. Rev. B* **66**, 115408 (2002).
21. D. Schlößer, K. Morgenstern, L.K. Verheij, G. Rosenfeld, F. Besenbacher, and G. Comsa, *Surf. Sci.* **465**, 19 (2000).
22. Y. W. Mo, J. Kleiner, M. B. Webb, and M. G. Lagally, *Phys. Rev. Lett.* **66**, 1998 (1991).
23. H. Brune, H. Röder, C. Boragno, and K. Kern, *Phys. Rev. Lett.* **73**, 1955 (1994).
24. H. Brune, H. Röder, K. Bromann, and K. Kern, *Thin Solid Films* **264**, 230 (1995).
25. H.H. Teng, P.M. Dove, C.A. Orme, and J.J. De Yoreo, *Science* **282**, 724 (1998).
26. C.M. Pina, U. Becker, P. Risthaus, D. Bosbach, and A. Putnis, *Nature* **395**, 483 (1998).
27. E. Bauer, *Rep. Prog. Phys.* **57**, 895 (1994).
28. A.K. Schmidt, N.C. Bartelt, and R.Q. Hwang, *Science* **290**, 1561 (2000).
29. J.B. Hannon and R.M. Tromp, *Annual Review of Materials Research*, **33**, 263 (2003).
30. G. Ertl and H.H. Rotermund, *Current Opinion in Solid State and Materials Science* **1**, 617 (1996).
31. C.M. Schneider and G. Schönhense, *Rep. Prog. Phys.* **65**, 1785 (2002).
32. M. Zinke-Allmang, L.C. Feldman, and M.H. Grabow, *Surf. Sci. Rep.* **16**, 377 (1992).
33. M. Zinke-Allmang, *Thin Solid Films* **346**, 1 (1999).
34. R. M. Tromp and J. B. Hannon, *Surf. Rev. Lett.* **9**, 1565 (2002).
35. H.-C. Jeong and E.D. Williams, *Surf. Sci. Rep.* **34**, 171 (1999).
36. M. Giesen, *Prog. Surf. Sci.* **68**, 1 (2001) and references therein.
37. M. Nowicki, A. Emundts, and H. P. Bonzel, *Prog. Surf. Sci.* **74**, 123 (2003).
38. H. P. Bonzel, *Phys. Rep.* **385**, 1 (2003).

39. F.H. Baumann, D.L. Chopp, T. Díaz de la Rubia, G. H. Gilmer, J.E. Greene, H. Huang, S. Kodambaka, P. O'Sullivan, and I. Petrov, *MRS Bull.* **26**, 182 (2001).
40. S. Kodambaka, S.V. Khare, I. Petrov, J.E. Greene. *Surface Science Reports* **60**, 55 (2006).
41. I. Petrov, F. Adibi, J.E. Greene, W.D. Sproul, and W.-D. Münz, *J. Vac. Sci. Technol. A* **10**, 3283 (1992).
42. S. Kodambaka, S.V. Khare, V. Petrova, A. Vailionis, I. Petrov, and J.E. Greene, *Surf. Sci.* **513**, 468 (2002).
43. S. Kodambaka, V. Petrova, S.V. Khare, D. Gall, A. Rockett, I. Petrov, J.E. Greene, *Phys. Rev. Lett.* **89**, 176102 (2002).
44. S. Kodambaka, N. Israeli, J. Bareño, W. Święch, K. Ohmori, I. Petrov, and J.E. Greene, *Surf. Sci.* **560**, 53 (2004).
45. S. Kodambaka, J. Bareño, S.V. Khare, W. Swiech, I. Petrov, J.E. , Greene, *J. Appl. Phys.* **98**, 34901 (2005).
46. Image SXM, developed by Prof. Steve Barrett, Liverpool, UK (http://www.liv.ac.uk/~sdb/ImageSXM/).
47. W.W. Mullins, *Interface Sci.* **9**, 9 (2001) and references therein.
48. J.G. McLean, B. Krishnamachari, D.R. Peale, E. Chason, J.P. Sethna, and B.H. Cooper. *Phys. Rev. B* **55**, 1811 (1997).
49. L. Kuipers, M.S. Hoogeman, J.W.M. Frenken, and H. van Beijeren, *Phys. Rev. B* **52**, 11387 (1995).
50. C. Pearson, B. Borovsky, M. Krueger, R. Curtis, and E. Ganz. *Phys. Rev. Lett.* **74**, 2710 (1995).
51. *CRC Handbook of Chemistry and Physics*, 82nd edition 2001-2002, pp. 4.
52. S. Kodambaka, V. Petrova, S.V. Khare, D.D. Johnson, I. Petrov, and J.E. Greene, *Phys. Rev. Lett.* **88**, 146101 (2002).
53. W.K. Burton, N. Cabrera, and F.C. Frank, *Philos. Trans. R. Soc. London A* **243**, 299 (1951).
54. S. Tanaka, N.C. Bartelt, C.C. Umbach, R.M. Tromp, and J.M. Blakely, *Phys. Rev. Lett.* **78**, 3342 (1997).
55. K. Thürmer, J.E. Reutt-Robey, E.D. Williams, M. Uwaha, A. Emundts, and H.P. Bonzel, *Phys. Rev. Lett.* **87**, 186102 (2001).
56. K.F. McCarty, J.A. Nobel, and N.C. Bartelt, *Nature* **412**, 622 (2001).
57. A. Rettori and J. Villain, *J. Phys. (France)* **49**, 257 (1988).
58. N. Israeli and D. Kandel, *Phys. Rev. Lett.* **80**, 3300 (1998).
59. N. Israeli and D. Kandel, *Phys. Rev. B* **60**, 5946 (1999).
60. M. Giesen, G. Schulze Icking-Konert, and H. Ibach, *Phys. Rev. Lett.* **80**, 552 (1998).
61. K. Thürmer, J.E. Reutt-Robey, E.D. Williams, M. Uwaha, A. Emundts, and H.P. Bonzel, *Phys. Rev. Lett.* **87**, 186102 (2001).
62. K. Morgenstern, G. Rosenfeld, G. Comsa, M.R. Sørensen, B. Hammer, E. Lægsgaard, and F. Besenbacher, *Phys. Rev. B* **63**, 045412 (2001).
63. S. Kodambaka, S. V. Khare, V. Petrova, D.D. Johnson, I. Petrov, and J.E. Greene, *Phys. Rev. B* **67**, 035409 (2003).
64. S. Kodambaka, S.V. Khare, W. Święch, K. Ohmori, I. Petrov, and J.E. Greene, *Nature* **429**, 49 (2004).
65. V. Bulatov, F.F. Abraham, L. Kubin, B. Devincre, and S. Yip, *Nature* **391**, 669 (1998).
66. B.W. Lagow, I.M. Robertson, M. Jouiad, D.H. Lassila, T.C. Lee, and H.K. Birnbaum, *Material Science & Engineering A*. **309-310**, 445-450 (2001).
67. A.R. Verma and S. Amelinckx, *Nature* **167**, 939 (1951).
68. N. Cabrera and M.M. Levine, *Phil. Mag.* **1**, 450 (1956).
69. T. Surek, G.M. Pound, and J.P. Hirth, *Surf. Sci.* **41**, 77 (1974).
70. S.-J. Tang, S. Kodambaka, W. Święch, I. Petrov, C.P. Flynn, and T.C. Chiang, *Phys. Rev. Lett.* **96**, 126106 (2006).
71. R.M. Tromp and M.C. Reuter, *Ultramicroscopy* **36**, 99 (1991).
72. F.C. Frank and W.T. Read, *Phys. Rev.* **79**, 722 (1950).
73. J. Bardeen and C. Herring in *Imperfections in Nearly Perfect Crystals,* edited by W. Shockley, J.H. Hollomon, R. Maurer, and F. Seitz, New York: Wiley, 1952.
74. D. Hull and D.J. Bacon, in *Introduction to Dislocations,* Oxford: Pergamon Press, 1984.
75. J.E. Sundgren, B.O. Johansson, A. Rockett, S.A. Barnett, and J.E. Greene, in *Physics and Chemistry of Protective Coatings,* edited by J.E. Greene, W.D. Sproul, and J.A. Thornton, American Institute of Physics, New York, 1986.
76. D. Gall, S. Kodambaka, M.A. Wall, I. Petrov, and J.E. Greene, *J. Appl. Phys.* **93**, 9086 (2003).
77. J. Weertman and J.R. Weertman, in *Elementary Dislocation Theory*, edited by M.E. Fine, J. Weertman, and J.R. Weertman, New York: Macmillan Company, 1964.
78. J.F. Justo, M. de Koning, W. Cai, and V.V. Bulatov, *Material Science & Engineering A* **309-310**, 129 (2001).
79. T. Surek, J.P. Hirth, and G.M. Pound, *Journal of Crystal Growth* **18**, 20 (1973).
80. V.L. Indenbom and Z.K. Saralidze, in *Elastic Strain Fields and Dislocation Mobility,* edited by V. Indenbom and J. Lothe, Amsterdam: Elsevier Science,1992.